Biophysical Journal, Volume 98

Supporting Material

An Electrostatic Model for DNA Surface Hybridization

Ian Y. Wong and Nick Melosh

Supporting Material

An Electrostatic Model for DNA Surface Hybridizatoin

Ian Y. Wong and Nicholas A. Melosh

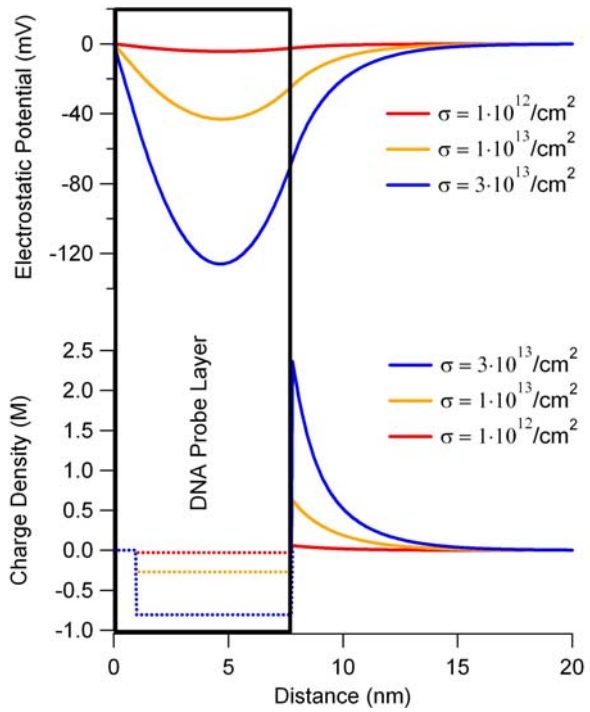

Supplemental Figure 1. **Electrostatic potential field and charge density profile near a DNA probe layer of varying grafting densities** ($\sigma = 1{\cdot}10^{12}/cm^2$, $1{\cdot}10^{13}/cm^2$ and $3{\cdot}10^{13}/cm^2$) at a bulk salt concentration of [NaCl] = 0.3 M. The DNA oligo length is $N = 20$ bp, which corresponds to $H = 7.8$ nm for a 1 nm surface linker and a spacing of 0.34 nm/bp. The boundary condition is given by $V(x = 0) = 0$ mV. As probe density increases, the charge density of the layer also increases, resulting in stronger electrostatic potentials and stronger counterion screening outside the layer.

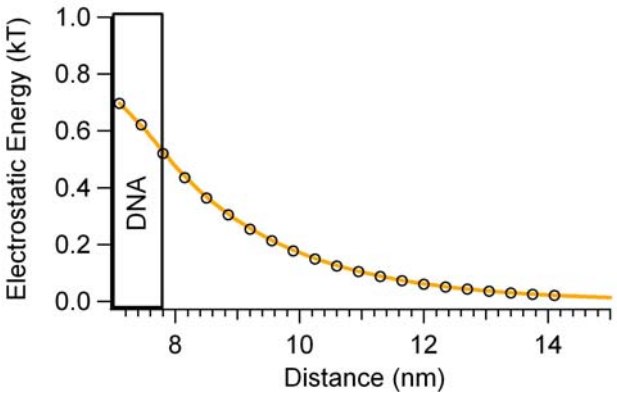

Supplemental Figure 2. **Electrostatic energy associated with partially inserting a 20-bp DNA oligo target into a DNA probe layer** with grafting densities $\sigma = 10^{13}/cm^2$ at a bulk salt concentration of [NaCl] = 0.3 M. Black circles correspond to the location of the negative charges on the target backbone; the electrostatic energy at each position is

summed to calculate the total electrostatic barrier to hybridization. This is equivalent to taking the convolution of the electrostatic potential field with an overlapping step-function whose width is the contour length of DNA. Shifting the position of this step function does not significantly affect the trends determined using this model. Similarly, using a Gaussian monomer distribution instead of a uniform distribution also yields similar trends, since for short oligomers the number of Kuhn segments N is small and the contour length (aN) is comparable to the RMS end-to-end distance ($aN^{1/2}$). In this case, the total electrostatic barrier $\Delta G_a \sim 4.5\ k_B T$.

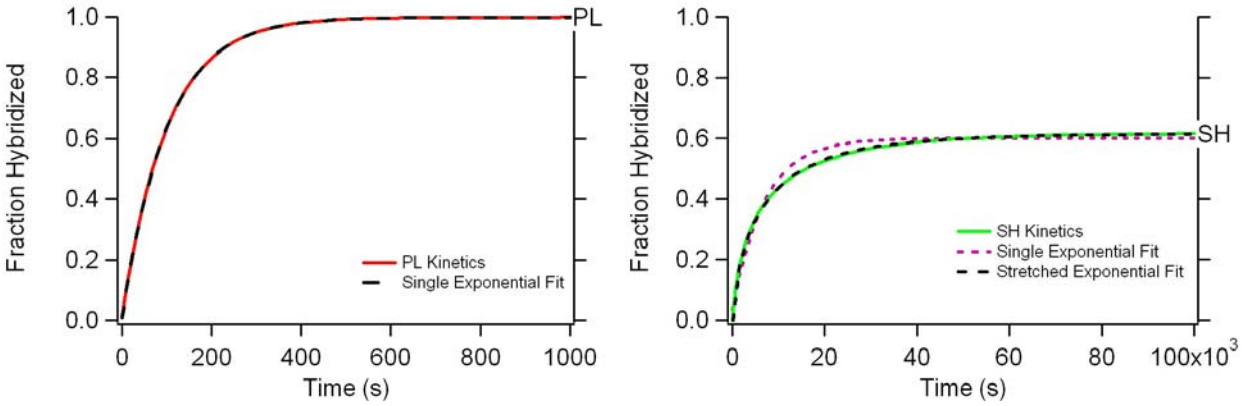

Supplemental Figure 3. **Single and stretched-exponential fits of hybridization kinetics from Figure 3** at varying probe densities and a bulk salt concentration of [NaCl] = 0.3 M. In the PL regime with $\sigma = 10^{12}/cm^2$, the hybridization kinetics are well-fit by a single-exponential with a characteristic timescale $\tau = 100$ s. However, in the SH regime with $\sigma = 10^{13}/cm^2$, the hybridization kinetics are poorly fit by a single-exponential with a characteristic timescale of $\tau = 6972$ s, due to the distribution of electrostatic barriers. Instead, the hybridization kinetics are well fit by a stretched exponential of the form $\exp[-(t/\tau)^{\alpha}]$ where $\tau = 7174$ s and $\alpha = 0.67$.

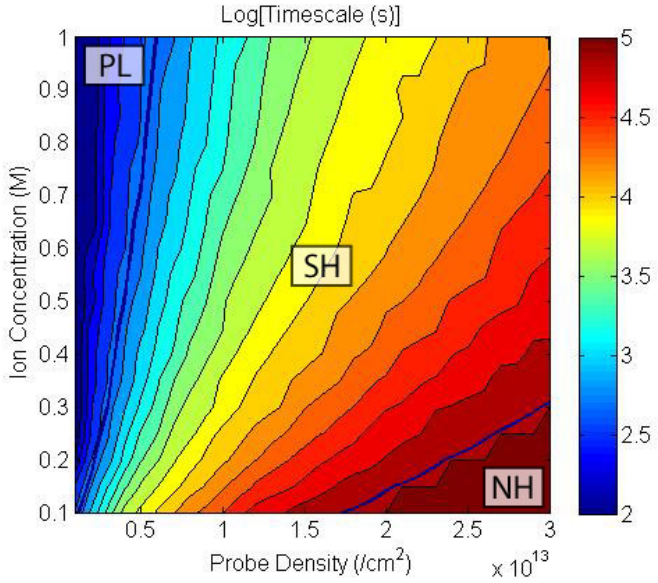

Supplemental Figure 4. **Characteristic timescales of DNA hybridization as a function of probe density and ion concentration**, defined as reaching 63% of the steady state value and logarithmically spaced. In the pseudo-Langmuir (PL) regime of low probe densities and high ionic salt concentrations, electrostatic barriers are low, so hybridization occurs in the fast limit $\tau_{fast} \sim (k_{on} C_T)^{-1} = 10^2$ s. In the no hybridization (NH) regime of high probe densities and low ionic salt concentrations, electrostatic barriers are high, so hybridization occurs in the slow limit

$\tau_{slow} \sim k_{off}^{-1} = 10^5$ s. The suppressed hybridization (SH) regime corresponds to intermediate probe densities and ionic salt concentrations, so the characteristic timescales range between these fast and slow limits.

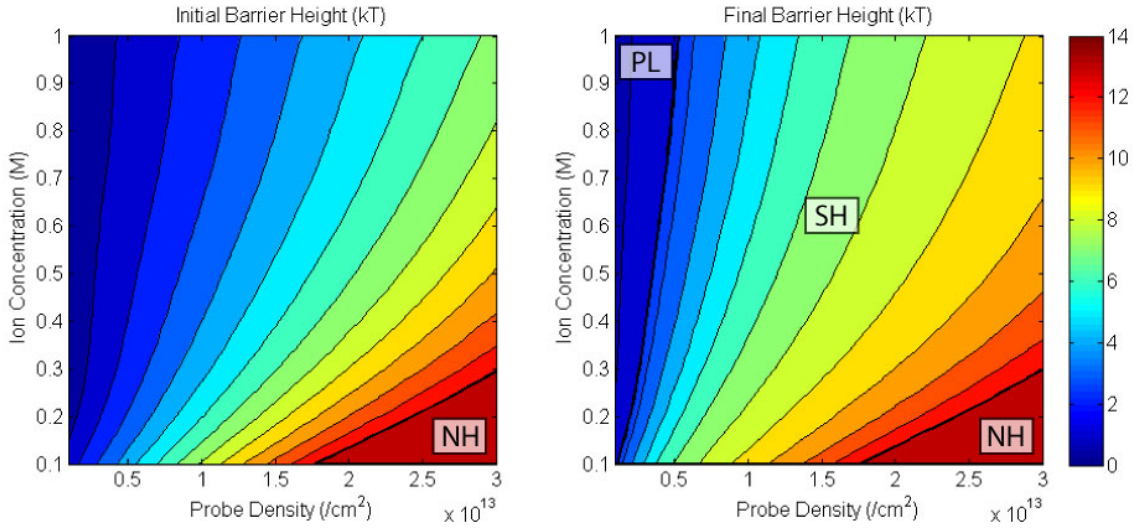

Supplemental Figure 5. (*Left*) **Initial electrostatic barrier as a function of probe density and ion concentration**. The no hybridization (NH) regime occurs at high probe densities and low ion concentrations when $\Delta G_a \geq 13\ k_B T$, which corresponds to $\leq 1\%$ hybridization. (*Right*) **Final electrostatic barrier (after hybridization reaches steady-state) as a function of probe density and ion concentration**. The NH regime is unchanged since no hybridization occurs, but the PL regime occurs at low probe densities and high ion concentrations where $\Delta G_a \leq 2.5\ k_B T$, which corresponds to 99% hybridization. Note that the SH/NH boundary remains the same both before and after hybridization since minimal hybridization occurs.

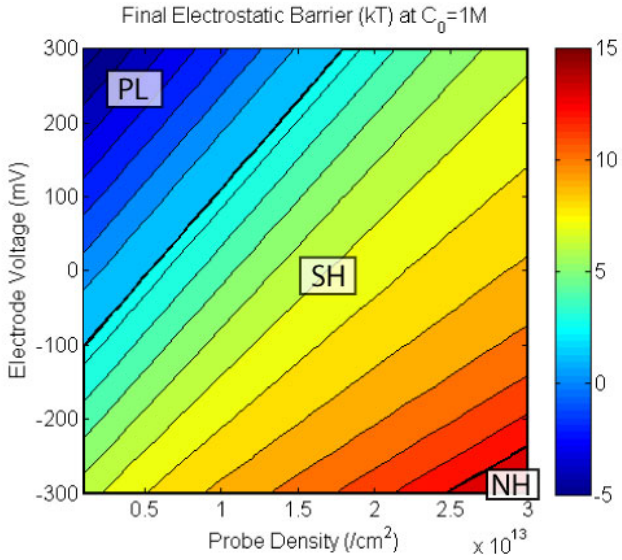

Supplemental Figure 6. **Final electrostatic barrier (after hybridization reaches steady-state) as a function of probe density and applied voltage** at fixed ion concentration $C_0 = 1$M. The no hybridization (NH) regime occurs at high probe densities and negative voltages when $\Delta G_a \geq 13\ k_B T$, which corresponds to $\leq 1\%$ hybridization. The PL regime occurs at low probe densities and positive voltages where $\Delta G_a \leq 2.5\ k_B T$, which corresponds to 99% hybridization. Note that when electrostatic barriers less than 1 kT, the hybridization rate constants reduce to the dilute limit.

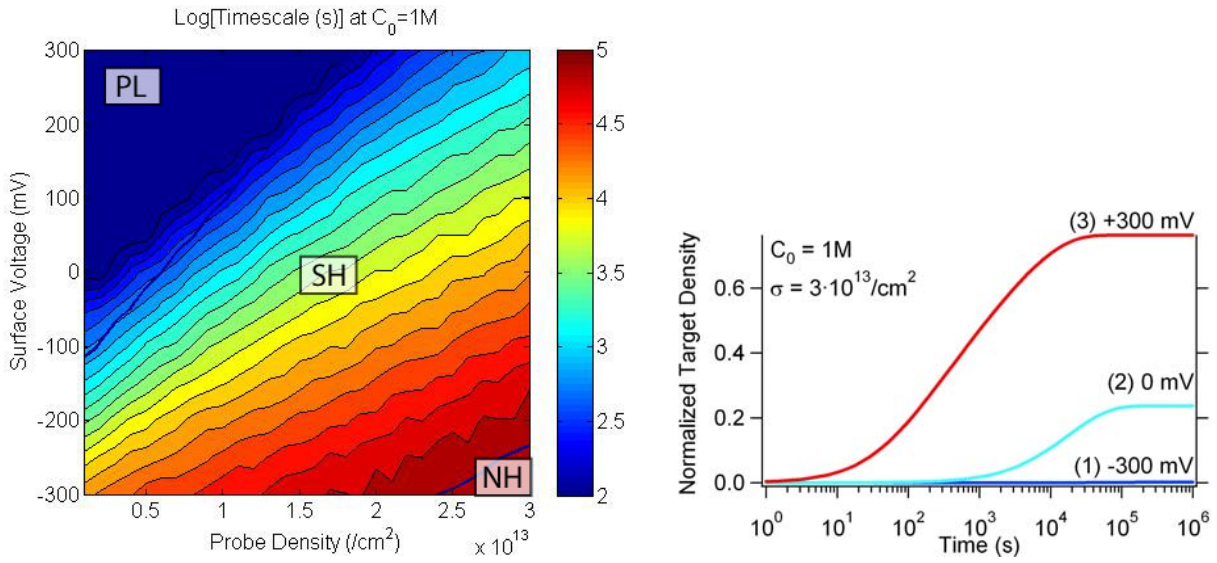

Supplemental Figure 7. (*Left*) **Characteristic timescales of DNA hybridization as a function of probe density and surface voltage**, defined as reaching 63% of the steady state value and logarithmically spaced. In the pseudo-Langmuir (PL) regime of low probe densities and positive voltages, electrostatic barriers are low, so hybridization occurs in the fast limit $\tau_{fast} \sim (k_{on}C_T)^{-1} = 10^2$ s. In the no hybridization (NH) regime of high probe densities and negative voltages, electrostatic barriers are high, so hybridization occurs in the slow limit $\tau_{slow} \sim k_{off}^{-1} = 10^5$ s. The suppressed hybridization (SH) regime corresponds to intermediate probe densities and ionic salt concentrations, so the characteristic timescales range between these fast and slow limits. (*Right*) **Normalized hybridization kinetics at applied voltages of V = -300 mV, 0 mV and +300 mV**, respectively for the high probe density limit of $\sigma_P = 3\cdot10^{13}/cm^2$ and high fixed ion concentration C_0 = 1M, corresponding to points 1, 2, and 3 in Fig. 6, right. Despite the higher hybridization density +300 mV, the kinetics are about an order of magnitude faster than at 0 mV.

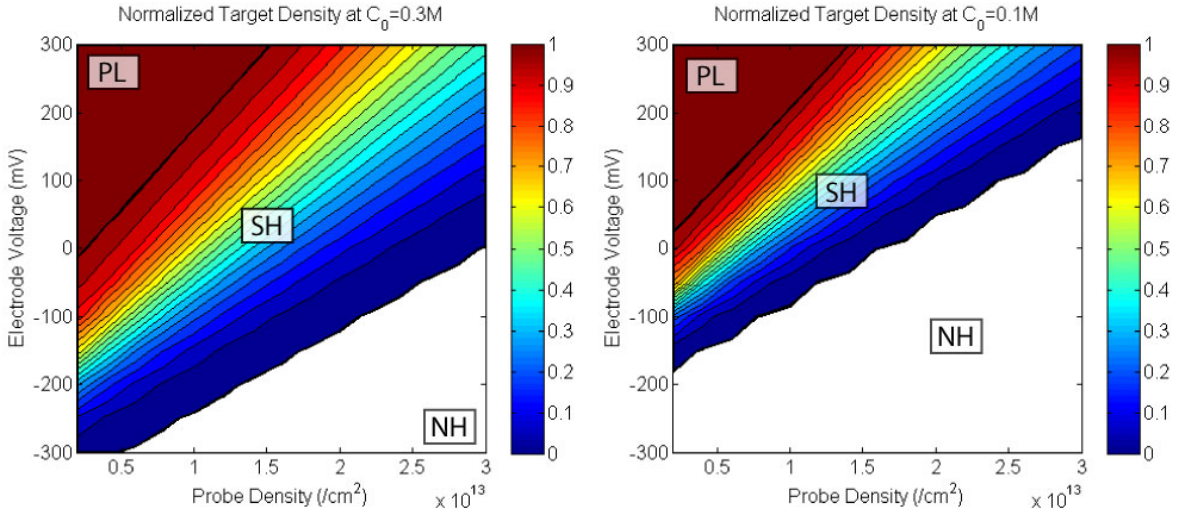

Supplemental Figure 8. **Normalized hybridization as a function of probe density and applied voltages at ion concentration C_0 = 0.3M** (*left*) **and C_0 = 0.1M** (*right*). Decreased counterion screening at lower ionic salt concentrations leads to higher electrostatic barriers and shifts the PL/SH and SH/NH boundaries to more positive voltages and lower probe densities.

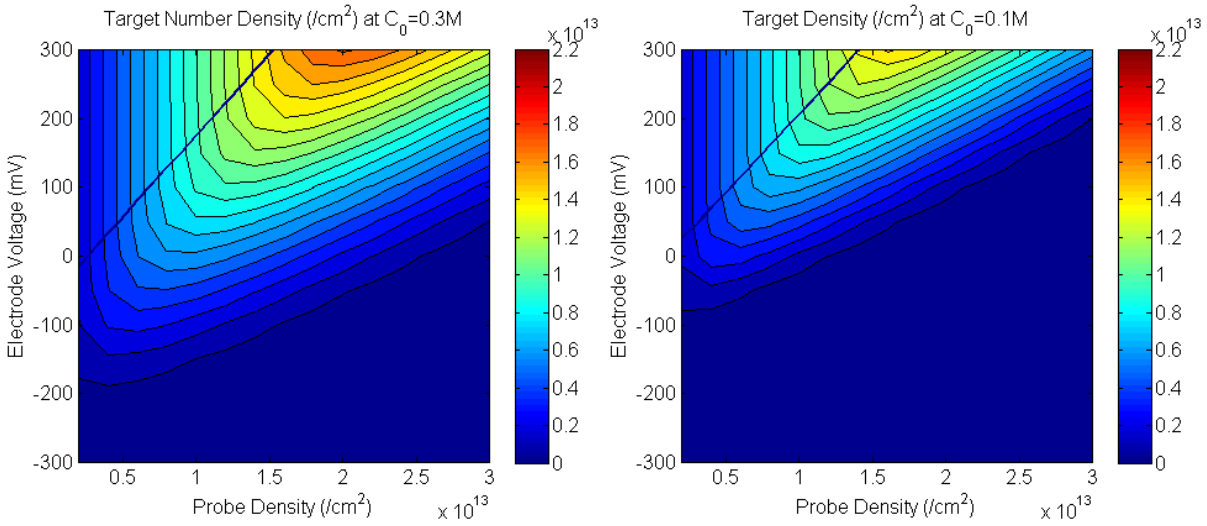

Supplemental Figure 9. **Hybridized target number density as a function of probe density and applied voltages at ion concentration C_0 = 0.3M** (*left*) **and C_0 = 0.1M** (*right*). At lower ionic salt concentrations, the optimum probe density is shifted to lower values and corresponds to a smaller hybridized target number density.

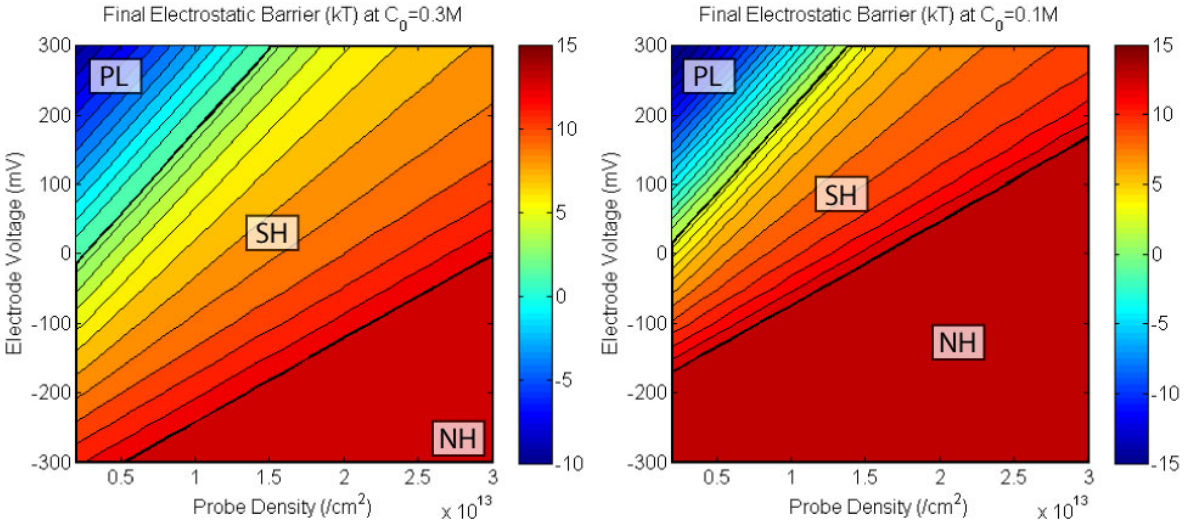

Supplemental Figure 10. **Final electrostatic barrier (after hybridization reaches steady-state) as a function of probe density and applied voltages at ion concentration C_0 = 0.3M** (*left*) **and C_0 = 0.1M** (*right*). Decreased counterion screening at lower ionic salt concentrations leads to higher electrostatic barriers and shifts the PL/SH and SH/NH boundaries to more positive voltages and lower probe densities. The no hybridization (NH) regime occurs at high probe densities and negative voltages when $\Delta G_a \geq 13\ k_B T$, which corresponds to $\leq$ 1% hybridization. The PL regime occurs at low probe densities and positive voltages where $\Delta G_a \leq 2.5\ k_B T$, which corresponds to 99% hybridization. Note that when electrostatic barriers less than 1 kT, the hybridization rate constants reduce to the dilute limit.

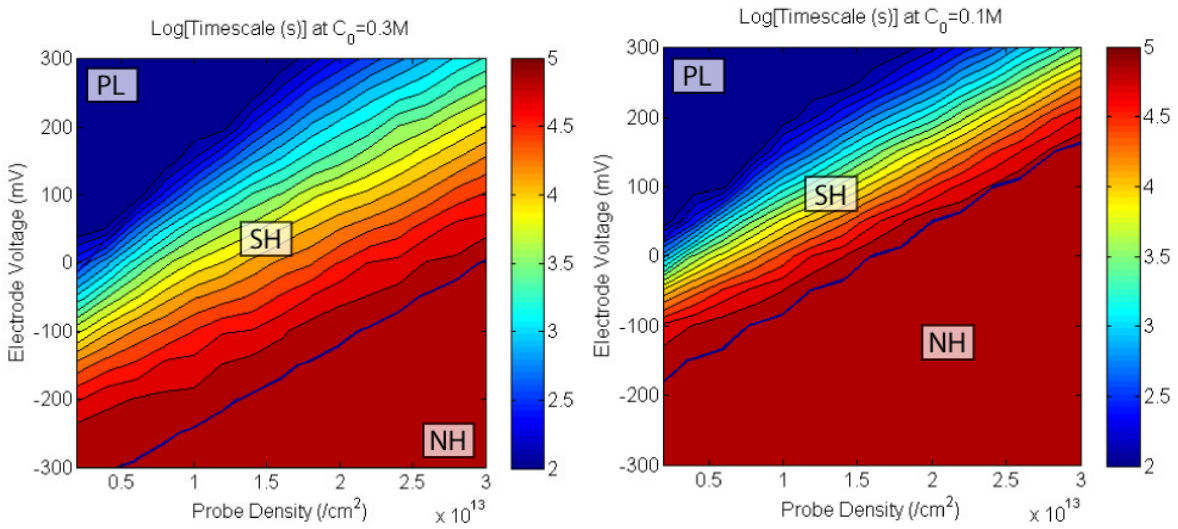

Supplemental Figure 11. **Characteristic timescales of DNA hybridization as a function of probe density and applied voltages at ion concentration C_0 = 0.3M** (*left*) **and C_0 = 0.1M** (*right*), defined as reaching 63% of the steady state value and logarithmically spaced. Decreased counterion screening at lower ionic salt concentrations leads to higher electrostatic barriers, which slow down hybridization kinetics in the SH and NH regimes.

Discussion: Electrostatic Model with Variable Heights

The electrostatic model implemented in the paper approximates the DNA brush layer as being strongly stretched with a constant brush height H = 7.8 nm (the sum of the contour length of a 20 bp dsDNA oligomer and a 1 nm alkanethiol linker). This strong-stretching approximation may not be appropriate in the limit of low probe densities or higher ion concentrations. To assess the validity of this approximation, a variant of this model was implemented that allowed for variable brush heights.

In polyelectrolyte brush theories, the scaling of the height on both the grafting density σ and bulk ion concentration C_0 can be divided into two regimes. In the "salted brush" regime, the salt concentrations inside and outside the brush are comparable. As a result, the brush height is dominated by excluded volume interactions between segments, leading to a relatively weak dependence of $H \sim (\sigma/C_0)^{1/3}$. However, in the "osmotic brush" regime, the salt concentration (of trapped counterions) is considerably higher inside the brush, leading to a brush height that is independent of σ and C_0.

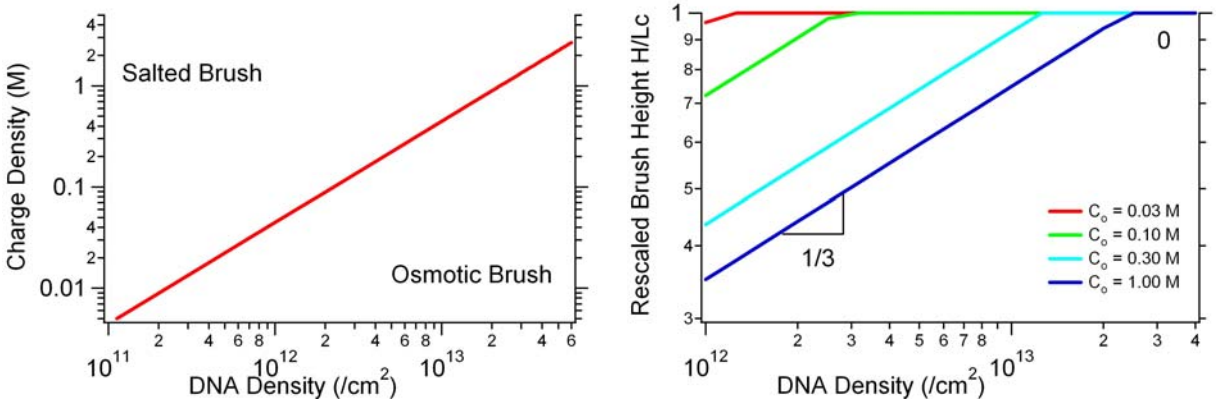

Supplemental Figure 12. (*Left*) **Approximate charge density (in M) associated with a particular DNA grafting density (in /cm^2)**, which demarcates the transition from salted brush to osmotic brush regimes. (*Right*) **Approximate brush height at varying probe densities and bulk salt concentrations.** In the salted brush regime at low densities, the brush height scales weakly with as the ratio of grafting density to bulk salt concentration, $H \sim (\sigma/C_0)^{1/3}$. In the osmotic brush regime at higher densities, the brush height is largely independent of these two parameters.

Fig S12(left) shows the approximate conversion of DNA grafting density to charge density, which provides a straightforward way to determine the appropriate scaling regime for a given set of experimental parameters. Fig S12(right) shows the approximate brush heights at varying DNA densities at fixed salt concentrations. As bulk salt concentration increases, the salted brush regime spans a wider range of grafting densities. It should be noted, however, that the charge densities associated with this regime are relatively low, especially since there is a 45% reduction due to Manning condensation by immobile counterions.

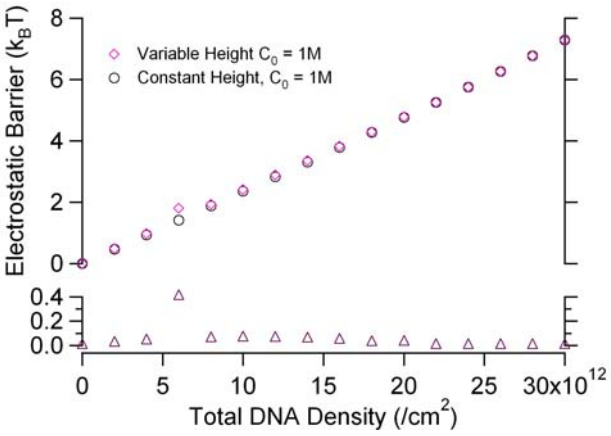

Supplemental Figure 13. **Scaling of electrostatic barrier ΔG_a with increasing DNA density at C_0 = 1M for electrostatic models assuming constant height (black) and variable height (magenta)**. These two models yield nearly identical trends since the charge densities are relatively low below in the low area density regime (<10^{13}/cm^2) where changes in height are most pronounced, so the electrostatic barriers are also relatively small (~ k_BT). Lower axis plots the difference between these two models.

Fig S13 compares the electrostatic barriers associated with inserting a DNA target 3 bp into a DNA probe layer of constant as well as variable height at a bulk salt concentration of C_0 = 1M, as well as the difference in the two (lower plot). The similarity between these models arises from two mechanisms. In the low-density salted brush regime, the height can be highly variable, allowing shorter heights and higher charge densities. However, the overall charge density is relatively low even at these reduced heights, so the electrostatic barriers are not significant. This corresponds to the pseudo-Langmuir regime where hybridization is driven to completion without appreciable electrostatic suppression. In the high-density osmotic brush regime, the height becomes constant, which recovers the behavior of the constant height model.

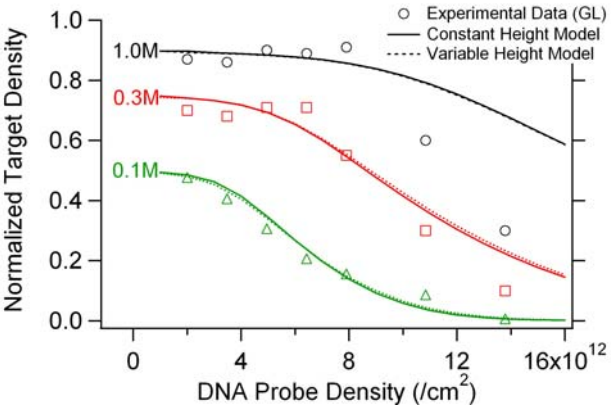

Supplemental Figure 14. **Comparison of normalized target density at varying probe densities, ion concentrations and zero voltage** (replotted from Figure 2). Markers are experimental data replotted from Gong and Levicky, continuous lines are results from the electrostatic model with constant height and dotted lines are results from the electrostatic model with variable height. Note that the constant height and variable height models are essentially identical since the differences in height at low density occur in the PL regime where electrostatic effects are weak.

Fig S14 shows experimental data from Gong and Levicky with the hybridization fractions calculated using both variable height and constant height models (other parameters same as Figure 2). Since the variable height and constant height models yield trends that are essentially identical, it is not necessary to incorporate variable height behavior for good agreement with experiment.

Discussion: Electrostatic Model with Variable Screening

The electrostatic model implemented in the paper approximates the DNA brush layer as being internally screened only by Manning condensed immobile counterions. This accounts for the somewhat unusual situation where DNA at sufficiently high grafting densities (as well as the associated immobile counterions and hydration layers) may occupy a significant portion of the available volume within the layer. As a result, it can be energetically unfavorable for additional counterions to enter the layer to screen additional hybridized DNA targets. This has been suggested as the mechanism preventing the onset of hybridization when the initial charge density σ associated with the probes is comparable to the bulk salt concentration C_0.

This approximation was validated by implementing a variant of the electrostatic model that allows for mobile counterion screening within the layer. In these modified models, an additional term corresponding to the modified Poisson-Boltzmann equation was added to [1] and [3] to treat counterion screening *within* the layer:

$$\rho_{Solution} = \left(\frac{C_0 \sinh(\psi)}{1 + 2\nu_h \sinh^2(\psi/2)} \right) \theta(H - x) \qquad [S1]$$

An important feature of this expression is the steric size parameter $\nu = 2C_0a^3$, which prevents the equation from diverging unphysically at large electrostatic potentials by limiting the maximum ion concentration to a^{-3}. In solution, this value was set to be $a^{-3} \sim 4.6$M. However, using this value within the DNA brush layer led to nearly complete screening of applied voltages within a few nanometers of the electrode surface and very small increases in layer charge density due to hybridization. Although this is physically reasonable in the limit of low DNA densities, this is not consistent with experimental results at higher DNA densities.

In order to reconcile the observed phenomena in both low and high DNA density regimes, the steric size parameter was weighted by the DNA density at any given time: $\nu = 2C_0a^3[1+100(\sigma_{DNA}/\sigma_{sat})]$, where σ_{DNA} is the total DNA density at any given time and σ_{sat} is a threshold "saturating" density where the volume within the layer is fully occupied by DNA and no additional mobile counterions can be incorporated. The free unoccupied volume within the layer can thus be estimated from $1 - (\sigma_{DNA}/\sigma_{sat})$. When the DNA density exceeds this saturating density, the steric size parameter ν is less than 1% of the solution steric size parameter, so that this term [S1] becomes negligible and the approximation of no mobile counterions is recovered.

Since it was unclear *a priori* what the saturating threshold density should be, the modified model was implemented for $\sigma_{sat} = 10^{13}/cm^2$, $3 \cdot 10^{13}/cm^2$ and $10^{14}/cm^2$. Fig S15 shows the maximum allowed counterion concentrations a^{-3} from the weighted steric size parameter ν_h for these three values of f_{sat}.

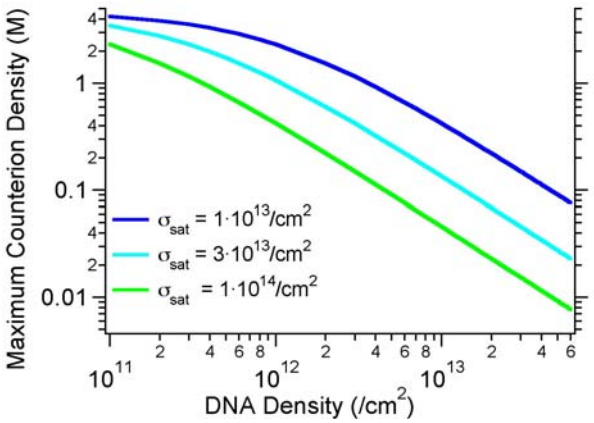

Supplemental Figure 15. **Scaling of maximum allowed counterion concentration in layer with DNA density for three** saturating densities of $\sigma_{sat} = 10^{13}/cm^2$, $3 \cdot 10^{13}/cm^2$ and $10^{14}/cm^2$. As DNA density increases, the available volume for additional mobile counterions decreases correspondingly. At the threshold values of DNA coverage, the allowed mobile counterion concentration is sufficiently small that the limiting case of no mobile counterions is recovered.

Fig S16 compares the electrostatic barriers associated with inserting a DNA target 3 nt into a DNA probe layer assuming no mobile counterions as well as using the saturating densities of $\sigma_{sat} = 10^{13}/cm^2$, $3 \cdot 10^{13}/cm^2$ and $10^{14}/cm^2$ at a bulk salt concentration of $C_0 = 0.1$M, as well as the differences between each model (lower plot). For DNA densities well below the threshold value, the electrostatic barriers calculated using the variable mobile counterion model are on the order of k_BT and much lower than the no mobile counterion model. It should be noted that these densities correspond to the pseudo-Langmuir regime, where the hybridization fraction is 100% and primarily limited by the probe density, so these differences between model variants are largely irrelevant. However, for DNA densities well above the critical threshold value, the electrostatic barrier converges to the limit of no mobile counterions. The existence of these two regimes generates the highly nonlinear behavior for electrostatic barrier with increasing DNA density in these modified models.

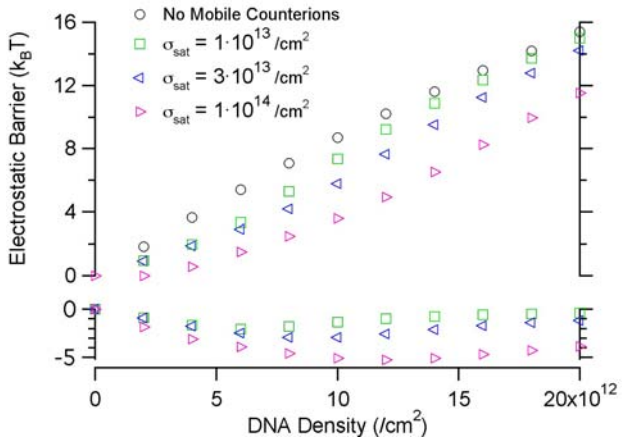

Supplemental Figure 16. **Scaling of electrostatic barrier ΔG_a with increasing DNA density at C_0 = 1M for electrostatic models assuming no mobile counterions (black) and variable mobile counterion concentrations with saturating densities of** saturating densities of $\sigma_{sat} = 10^{13}/cm^2$ (green), $3\cdot10^{13}/cm^2$ (blue) and $10^{14}/cm^2$ (magenta) at a bulk salt concentration of C_0 = 0.1M**.** These modified models exhibit highly nonlinear behavior with lower electrostatic barriers below the critical crossover density but recover the limit of no mobile counterions above the critical crossover density. Lower axis plots the differences between the no mobile counterion model and modified electrostatic models for each threshold value.

Fig S17 compares experimental data from Gong and Levicky with the the hybridization fractions calculated using no mobile counterions as well as the lowest saturating densities of $\sigma_{sat} = 10^{13}/cm^2$ (other parameters same as Figure 2, right). These two models yield qualitatively similar trends, particularly in the limit of high ion concentrations. Overall, the slightly lower electrostatic barriers in the variable mobile counterion model lead to slightly higher target hybridization fractions. These differences are least pronounced in the PL regime where hybridization is complete, but become more significant in the SH regime, although they never exceed 5%. This good agreement of the original model with no mobile counterions and the experimental data validates the approximation used. Nevertheless, these modified models may be useful in future work or other experimental systems as a way to fine-tune the transition from pseudo-Langmuir (PL) to suppressed hybridization (SH) in order to match experimental data, which may be difficult to accomplish using a purely linear dependence of electrostatic barrier on DNA density.

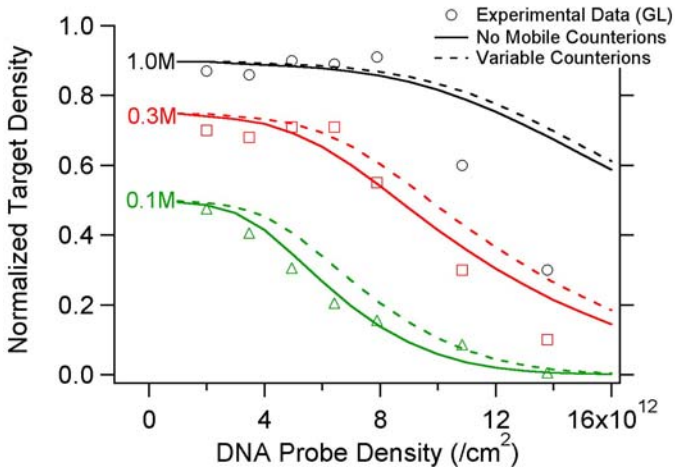

Supplemental Figure 17. **Comparison of normalized target density at varying probe densities, ion concentrations and zero voltage** (replotted from Figure 2). Markers are experimental data replotted from Gong and Levicky, continuous lines are results from the electrostatic model with no mobile counterions and dotted lines are results from the electrostatic model with variable mobile counterions and f_{sat} = 17%. The trends exhibited by these both models are qualitatively similar and have differences of less than 5% in hybridization.

Finally, we have selected that nucleation size (3 nt) and binding affinity (1-3 nM) to be in reasonable agreement with experiment. Deviating too far from these parameters produces trends that are difficult to reconcile with both zero voltage and positive voltage experiments. For example, requiring deeper insertion of 5 nt generates a very dramatic hybridization voltage dependence, leading to a 50-fold enhancement of hybridization at positive voltage, even with models allowing mobile counterions. Previous experiments show that this is not the case, and a model with a 3nt insertion and no mobile charges fits the data more accurately. Nevertheless, these choices may be worth revisiting in light of future experiments and molecular scale simulations.

Discussion: Empirical Modifications to Electrostatic Model

In the pseudo-Langmuir (PL) regime, the experimentally observed hybridization fractions in Gong and Levicky are constant but significantly less than 1. It is to be expected that the binding affinity (equilibrium constant) of DNA should become weaker at lower ion concentrations, consistent with measurements in dilute solution.

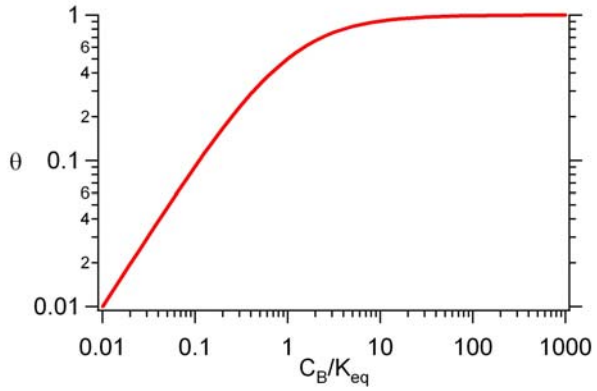

Supplemental Figure 18. **Langmuir isotherm for the steady state hybridization fraction θ_{ss} as a function of ε = C_B/K_D**. For strong binding affinities, 1 << ε and $\theta_{ss} \sim 1$. However, at weak binding affinities, ε << 1and $\theta_{ss} \sim \varepsilon$.

However, adjusting the binding affinities to match the experimentally measured values at low probe densities corresponds to the weak affinity regime (i.e. $C_B/K_D << 1$) in the Langmuir isotherm (S.Fig 18) where the steady-state hybridized fraction θ_{ss} becomes extremely sensitive to changes in C_B/K_D . Since k_{on} depends approximately exponentially on the hybridization density, even small increases in probe density cause strong suppression of hybridization, which is not consistent with the more gradual decrease in θ_{ss} in the suppressed hybridization (SH) regime.

The model can be made consistent with experimental measurements by constraining the maximum allowed hybridization density to values less than the probe density, i.e. $\frac{d\sigma}{dt} = k_{on} C_T (\eta\sigma_P - \sigma) - k_{off}\sigma$ where η = 0.9 for C_0 = 1M, η = 0.7 for C_0 = 0.3M etc. (Fig. S12)

Although this allows good agreement with experimental trends, it is difficult to justify this modification on physical grounds.